PERGAMON

International Journal of Heat and Mass Transfer 44 (2001) 3985–3995

International Journal of HEAT and MASS TRANSFER

www.elsevier.com/locate/ijhmt

Two-dimensional large-eddy simulation of turbulent natural convection due to internal heat generation

Andrej Horvat [a,*], Ivo Kljenak [a], Jure Marn [b]

[a] *Reactor Engineering Division, "Jožef Stefan" Institute, Jamova 39, SI-1000, Ljubljana, Slovenia*
[b] *Faculty of Mechanical Engineering, University of Maribor, Smetanova 17, SI-2000, Maribor, Slovenia*

Received 22 September 1999; received in revised form 5 February 2001

Abstract

Two-dimensional numerical simulations of laminar and turbulent natural convection in a fluid with internal heat generation in a square cavity are presented. The simulations were carried out at Rayleigh numbers 10^6–10^{11} and Prandtl numbers 0.25 and 0.6. The turbulent fluid motion was captured with a large-eddy simulation (LES) model. The Rayleigh–Taylor instabilities at the upper boundary and the Kelvin–Helmholtz instabilities at the side boundaries cause first local and then global transition from laminar to turbulent motion. Lower Prandtl numbers enhance heat transfer through the bottom region, whereas higher Prandtl numbers enhance heat transfer through the upper region of the simulation domain. The simulations also reveal that the Rayleigh–Nusselt number relation is not uniformly linear in a $\log_{10}$–$\log_{10}$ diagram.

Keywords: Heat transfer; Natural convection; Turbulence

1. Introduction

Natural convection is a widely studied heat transfer phenomenon. The reason for this particular interest is in the everyday importance of natural convection. It may be found practically anywhere where heat transfer is present in a fluid. Apart from the practical side, natural convection has also been studied as a classical dynamic system. Special attention has been focused on the transition to turbulence, which occurs under favorable conditions. Although natural convection due to internal heat generation is not less important, it drew much less attention in the past than the Rayleigh–Bénard convection, for example. However, in recent years, it became a subject of intense interest mainly due to nuclear safety issues. That is to say, in a light water reactor, an inadequate or prolonged absence of nuclear reactor core cooling may cause core melting to occur. The reactor core melt relocates, flowing downwards toward the reactor vessel lower plenum, where it accumulates. Heat is further generated in the melt pool due to fission product decay. To predict the behavior of the power plant and to design emergency procedures, it is necessary to know the dynamics and heat transfer processes in the radioactive melt pool. This is also a practical frame for the present work.

Investigations of natural convection phenomena in a fluid with volumetric heat generation began in the early 1970s with Kulacki and collaborators [1–3], who conducted several experiments using Joule heating as a volumetric heat source. In these experiments, which were primarily applicable to the nuclear industry, heat transfer through a horizontal fluid layer was assessed for different boundary cooling arrangements. Jahn and Reineke [4] and Steinberner and Reineke [5] experimentally and numerically investigated the natural convection of Joule-heated fluids in rectangular and semicircular cavities. The range of the Rayleigh number was from 5×10^5 to 3×10^{13} at the Prandtl number 7. They found that the natural convection flows in internally heated cavities are thermally stratified in the lower regions, whereas the upper part is unsteady due to a multi-vortex flow field. Using water as a working fluid,

* Corresponding author. Tel.: +386-1-588-54-50; fax: +386-1-561-23-35.
E-mail address: andrej.horvat@ijs.si (A. Horvat).

0017-9310/01/$ - see front matter
PII: S0017-9310(01)00066-7

Nomenclature

c_p	specific heat
Cn	convection term
C_s	Smagorinsky constant
Df	diffusion term
g	gravity
Gn	volumetric term
h	temperature
I	volumetric heat generation
l	filter width
L	length of simulation domain
Nu	Nusselt number
p	pressure
$Pr = c_p\rho v/\lambda$	Prandtl number
Ps	pressure term
$Ra = c_p\rho g\beta IL^5/\lambda^2 v$	Rayleigh number
$\underline{S}$	deformation velocity tensor
t	time
tDf	turbulent diffusion term
T	simulation time interval
v	velocity
x, y	spatial coordinates

Greek symbols

β	temperature dilatation
γ	finite volume boundary
ϵ	turbulent dissipation
λ	thermal conductivity
v	kinematic viscosity
ρ	mass density
$\underline{\tau}$	stress tensor
υ	thermal diffusivity

Subscripts/superscripts

b	domain boundary index
f	filter
i	finite volume boundary index
n	iteration index
sgd	subgrid or turbulent variable

Mayinger et al. [6] obtained experimentally as well as numerically the average heat transfer coefficient on the walls of rectangular and semicircular cavities. The investigated Rayleigh number spanned from 8×10^4 to 10^{11} at the Prandtl number 6–7. The researchers also conducted a numerical analysis to calculate the average heat transfer coefficient on the wall of spherical and vertical cylindrical cavities. Their published results demonstrated that the Prandtl number has a small effect on the Nusselt number. Asfia et al. [7] and Frantz and Dhir [8] also conducted experiments of natural convection in a spherical cavity. The working fluid was Freon-113, which was heated with microwaves. The range of the Rayleigh number tested was between 2×10^{10} and 1.1×10^{14} at the Prandtl number 8. These experiments confirm values of the Nusselt number, which were obtained by Mayinger et al. [6] 20 years earlier for a semicircular geometry. The influences of insulated and cooled pool top boundary were also assessed. In addition, it was observed that the ratio of maximum to minimum heat transfer coefficient can be as high as 20, while the ratio of maximum to average heat transfer can be as high as 2.5.

In all the above-mentioned experiments, the researchers were unable to reproduce adequate severe accident conditions. This was partly due to the high temperatures, which would be required, as well as the unknown material properties of the melt. The material properties of reactor core melt only recently have become known due to the RASPLAV project [9]. As a consequence, the Nusselt number correlations did not include the Prandtl number dependence. Later, numerical studies, which were conducted at the lower Prandtl numbers, confirmed the Prandtl number effect on the heat transfer processes on the walls of the simulation domain. In [10], the effect of the Prandtl number on the Nusselt number distributions for different geometries (rectangular, cylindrical and elliptical) was demonstrated. In their research, the Rayleigh number spanned from 10^6 to 10^{12} and the Prandtl number from 0.6 to 7. The authors found that the Prandtl number influence is small in convection-dominated regions and much more significant in conduction-dominated regions. Nevertheless, the influence of the Prandtl number on fluid behavior grows with the increase of the Rayleigh number. Also, Verzicco and Camussi [11] studied the Prandtl number effect on the dynamics of a convective turbulent flow with numerical experiments. They found that above the Prandtl number 0.35 the Nusselt number depends only on the Rayleigh number. However, the Prandtl number dependence of the Nusselt number was observed below the Prandtl number 0.35.

The common problem of all numerical simulations is the turbulent behavior of the fluid at high Rayleigh numbers, which was never successfully solved. Due to the small scale of fluid motion in the turbulent regime, additional modeling of turbulence is needed. Dinh and Nourgaliev [12] reviewed the turbulence modeling in large volumetrically heated liquid pools. The attention was focused on different k–ϵ models as well as on Reynolds stress models. Detailed calculations were performed for the CAPO experimental arrangement [13], where the cavity had a two-dimensional elliptical shape. The Rayleigh numbers were in the range from 10^6 to 10^{15}. Although the calculated results only slightly overpredict the Nusselt number values, the numerical

consistency of the model is questionable due to a very poor resolution of the numerical mesh. Furthermore, Wörner et al. [14] made a comprehensive study of turbulence in an internally heated convective fluid layer using direct numerical simulation. The Prandtl number of the modeled fluid was 7 and the Rayleigh numbers were in the range of 10^5–10^9. Using calculated turbulent moments and turbulent heat fluxes, the authors showed that the k–ϵ modeling is not suitable for the calculation of turbulent natural convection in a fluid with internal heat generation. As they were interested mainly in the turbulence data and wanted to save computational resources, their simulations were initiated from a parabolic temperature profile and were stopped before an overall thermal equilibrium was achieved. In our experience, this may lead to a severe underprediction of overall heat transfer over the simulation domain.

Some attempts to model the turbulent natural convection behavior in a fluid layer with internal heat generation were also presented in [15]. The calculations, which were performed for a fluid layer at Rayleigh numbers up to 1.4×10^9 with the Smagorinsky subgrid model, agreed well with the experimental data.

In the present paper, two-dimensional numerical simulations of laminar and turbulent natural convection in a fluid with internal heat generation in a square cavity are presented. The simulations were carried out at Rayleigh numbers of 10^6–10^{11} and the Prandtl numbers 0.25 and 0.6. The turbulent fluid motion was captured with the large-eddy simulation (LES) model. The performed simulations enable us to understand the time evolution of turbulent natural convection in fluids with a Prandtl number smaller than 1.0.

Based on numerical simulations, the time distributions of the Nusselt number on the cavity walls were also predicted. Comparison of the results for different Prandtl numbers shows a strong dependence of fluid dynamics on the Prandtl number.

2. Mathematical model

2.1. Transport equations

The basic assumption in the present work was that the fluid is incompressible with internal heat generation. To reduce the number of free parameters in the calculations and to simplify the comparison of results, the transport equations of mass, momentum and energy were transformed into a dimensionless form using Boussinesq's approximation to include buoyancy forces:

$$\nabla \cdot \vec{v} = 0, \tag{1}$$

$$\frac{\partial \vec{v}}{\partial t} + \nabla \cdot (\vec{v} \otimes \vec{v}) = -\nabla p + Pr(\nabla \cdot \underline{\tau}) - Ra\,Pr\,h\frac{\vec{g}}{|\vec{g}|}, \tag{2}$$

$$\frac{\partial h}{\partial t} + \nabla \cdot (\vec{v}h) = \nabla^2 h + 1. \tag{3}$$

A complete description of the scaling procedure may be found in [16,17].

At high Rayleigh numbers ($Ra > 10^8$), time-aperiodic behavior occurs. When the Rayleigh number is further increased, a local turbulent motion appears, reducing the local scale of fluid motion. To properly take the subgrid motion of the fluid into account, the LES Smagorinsky model was implemented, with a modification to capture the buoyancy forces due to the temperature gradients (as presented by Eidson [18]). After applying the LES concept of spatial filtering, Eqs. (1)–(3) can be written as:

$$\nabla \cdot \bar{\vec{v}} = 0, \tag{4}$$

$$\frac{\partial \bar{\vec{v}}}{\partial t} + \nabla \cdot \left(\bar{\vec{v}} \otimes \bar{\vec{v}}\right) = -\nabla \bar{p} + Pr\left(\nabla^2 \bar{\vec{v}}\right) - Ra\,Pr\,\bar{h}\frac{\vec{g}}{|\vec{g}|} + \nabla \cdot (v_{\mathrm{sgd}} 2\underline{\bar{S}}), \tag{5}$$

$$\frac{\partial \bar{h}}{\partial t} + \nabla \cdot \left(\bar{\vec{v}}\bar{h}\right) = \nabla^2 \bar{h} + 1 + \nabla \cdot \left(v_{\mathrm{sgd}} \nabla \bar{h}\right), \tag{6}$$

where the overbar indicates filtered values. The non-linear convection term of subgrid velocities in the momentum equation acts as a stress term with the artificial subgrid viscosity, which was modeled using the Kolmogorov assumption [19]:

$$v_{\mathrm{sgd}} = \mathrm{const.} f_{\mathrm{f}}^{4/3} \varepsilon^{1/3}. \tag{7}$$

It was further assumed that the filter splits the spectra of subgrid motion somewhere in the Kolmogorov equilibrium region and that subgrid turbulence dissipation is equal to subgrid turbulence production [21]. Using these assumptions, the subgrid turbulence production can be easily defined from filtered values. Thus,

$$v_{\mathrm{sgd}} = (C_{\mathrm{s}}\Delta x)^2 \left(2\underline{\bar{S}} : \underline{\bar{S}} + \frac{Ra\,Pr}{Pr_{\mathrm{sgd}}}\left(\nabla \bar{h} \cdot \frac{\vec{g}}{|\vec{g}|}\right)\right)^{1/2}. \tag{8}$$

The first term in Eq. (8) represents stress forces while the second term represents buoyancy. The constant C_{s} in Eq. (8) is case-dependent and must be determined empirically. In our case, its value was prescribed as 0.1, whereas the turbulent Prandtl number Pr_{sgd} was set equal to 0.4. Similarly, the non-linear convection term of subgrid velocities and temperature in the energy equation (6) can be replaced with diffusive flux using the subgrid thermal diffusivity defined as a linear function of subgrid viscosity:

$$v_{\mathrm{sgd}} = \frac{v_{\mathrm{sgd}}}{Pr_{\mathrm{sgd}}}. \tag{9}$$

The adopted Smagorinsky model is too dissipative in the vicinity of the walls. To reduce the near-wall dissipation, the subgrid viscosity was multiplied by the Van Driest damping function. Its theoretical background is described in [20].

The proposed turbulence model was chosen because of its simplicity and efficiency. The described procedure for obtaining subgrid viscosity (8) and subgrid thermal diffusivity (9) can be applied to transport equations (1)–(3) in two as well as in three dimensions. The absence of the vorticity stretching effect in two-dimensional turbulence significantly changes the path of the turbulence energy cascading process, yet it does not contradict the initial assumption of equality between subgrid turbulence production and subgrid turbulence dissipation, that is, the vortex stretching mechanism is responsible for redistribution of turbulent kinetic energy between dimensions. Furthermore, it is negligible on the subgrid-scale level if the applied spatial filter is small enough.

The applied turbulence model dampens the whole spectrum of subgrid motion and does not allow any energy backscatter. The dynamic LES models developed by Germano et al. [21] and Lilly [22] also allow energy backscatter from the subgrid to the resolved scales. The methods use spatial filtering on two grid levels to calculate the spatially dependent model constant C_s. As the filtering procedure is carried out explicitly, the dynamic LES model is easily applicable only on equidistant and structured meshes. This fact severely limits the range of suitable engineering problems. In [23], an attempt to use a dynamic LES model for the Rayleigh–Bénard convection is presented. They proposed an improvement of Eidson's formulation [18] of turbulent viscosity. As their assumptions violate the subgrid kinetic energy transport equation, the innovation was not applied in our model.

2.2. Geometrical considerations

Although experimental and numerical results for spherical and elliptical cavities are already available [24], a square cavity was used to simplify calculations at high Rayleigh numbers. A comparison of experimental results from natural convection cases in rectangular and spherical cavities reveals the similarity of heat transfer processes in both geometries. Moreover, it is safe to assume that the maximum Nusselt number is similar for rectangular and spherical cavities of similar dimensions. The maximum Nusselt number occurs in the upper corners of the cavities. Larger discrepancies between heat transfer in rectangular and spherical cavities occur only in the lower parts due to impingement and additional looping of the fluid caused by the corners [10,25].

Experimental and numerical results presented by Nourgaliev et al. [10] and Dinh and Nourgaliev [12] suggest that the fluid pattern is basically two-dimensional. Questioning this assumption, Wörner et al. [14] performed direct numerical simulations of a fluid layer with volumetric heat generation. These simulations show that the thermal field and the induced velocity field are three-dimensional and periodic in a spanwise direction, forming vertical convection cells of irregular forms. Taking into account the periodicity of fluid structures in a spanwise direction, a two-dimensional model reveals the basic characteristics of the considered phenomena.

2.3. Initial and boundary conditions

At the beginning of the simulation, the fluid was considered at rest and isothermal, with mean temperature $h = 0$. Random temperature fluctuations with an amplitude 10^{-6} were superimposed on the initial mean profile. For the momentum equation, no-slip boundary conditions at all boundaries of the square cavity were prescribed. To represent the solidification and melting processes on the walls of the lower plenum, identical isothermal boundary conditions at all boundaries were prescribed for the energy equation. During the entire simulation time interval, the dimensionless boundary temperature was $h = 0$.

3. Numerical procedure

3.1. Numerical mesh

The transport equations (4)–(6) were transformed into an integral form in order to force momentum and energy conservation. The discretization followed the finite volume method using 256×256 numerical cells. A staggered arrangement for grid points was applied. The thermal dissipation scale was estimated according to Arpaci [26] with Eq. (10), whereas for the calculation of the kinematic dissipation scale Eq. (11) was used.

$$\ell_{\text{thermal}} = \left(\frac{Pr+1}{PrRa}\right)^{1/4} L, \tag{10}$$

$$\ell_{\text{kinematic}} = \left(\frac{Pr^2}{Ra}\right)^{1/4} L. \tag{11}$$

As the test calculations revealed, the thickness of the boundary layer at the walls of the simulation domain is only 3–5 dissipation scales. In the cases of $Ra = 10^9$ and 10^{11}, a uniform numerical mesh with 256×256 grid points was still not able to capture the boundary layer flow. To enhance the resolution of the numerical model, the numerical mesh was locally refined to a point where the grid spacing near the boundaries was as small as the smallest dissipation scale.

3.2. Discretization techniques

The convection terms in the momentum (5) and energy (6) equations were discretized according to the high-resolution method as defined in [27]. As a limiter, the so-called "superbee" limiter was used. For the diffusion terms, the central-symmetric discretization was applied.

In time, the momentum (5) and energy (6) equations were discretized according to the semi-implicit Cranck–Nicholson scheme:

$$\vec{v}^{n+1} = \vec{v}^{n} - \Delta t[Cn^{n} + Ps^{n}] + \frac{\Delta t}{2}[(Df^{n} + Df^{n+1}) + (tDf^{n} + tDf^{n+1}) + (Gn^{n} + Gn^{n+1})], \tag{12}$$

$$\bar{h}^{n+1} = \bar{h}^{n} - \Delta t[Cn^{n}] + \frac{\Delta t}{2}[(Df^{n} + Df^{n+1}) + (tDf^{n} + tDf^{n+1})] + \Delta t, \tag{13}$$

whereas integration was performed with the Gauss–Siedel overrelaxation method as described in [28].

For the pressure calculation, the pressure correction method as found in [29] was applied. The elliptic pressure equation, which arises from the mass conservation principle combining Eqs. (4) and (5), was solved with the full multigrid method as proposed in [30].

3.3. Stability

The timestep for the time integration method was based on the stability restrictions for the explicit upwind and Lax–Wendroff schemes, which combined into the high-resolution scheme. For the momentum equation (5), the following stability conditions for the upwind scheme were implemented in the computational algorithm:

$$\Delta t\left[\frac{|v_x|}{\Delta x} + \frac{|v_y|}{\Delta y} + 2(v + v_{\mathrm{sgd}})\left(\frac{1}{\Delta x^2} + \frac{1}{\Delta y^2}\right)\right]_{j,i} = 0.25, \tag{14}$$

$$\Delta t\left[\frac{v_x^2}{|v_x|\Delta x + (v + v_{\mathrm{sgd}})} + \frac{v_y^2}{|v_y|\Delta y + (v + v_{\mathrm{sgd}})}\right]_{j,i} = 1, \tag{15}$$

whereas for the Lax–Wendroff scheme the stability of time integration was assured with

$$\Delta t\left[\left(\frac{v_x^2}{\Delta x^2} + \frac{v_y^2}{\Delta y^2}\right)\Delta t + (v + v_{\mathrm{sgd}})\left(\frac{1}{\Delta x^2} + \frac{1}{\Delta y^2}\right)\right]_{j,i} = 0.25. \tag{16}$$

As the timestep Δt in the last stability condition (16) cannot be expressed explicitly, the timestep from the previous iteration was used in the expression. For Δx and Δy, the smallest grid spacings were used.

The identical stability conditions were also implemented for the energy equation (6), where thermal diffusivity υ was used instead of viscosity v.

4. Results and discussion

Numerical simulations were performed for the Rayleigh numbers 10^6, 10^7, 10^8, 10^9 and 10^{11}. The Prandtl numbers were 0.25 and 0.6 in all cases. For the Rayleigh number $Ra = 10^6$, the dimensionless simulation time T was 0.3, for $Ra = 10^7$ T was 0.2, for $Ra = 10^8$ T was 0.1, for $Ra = 10^9$ T was 0.05 and for $Ra = 10^{11}$ T was 0.015. Fig. 1 presents snapshots of the temperature field for different combinations of Rayleigh and Prandtl numbers at the end of the simulation time T. Simulated velocity fields were also observed to examine the flow structures.

In general, the internally heated fluid rises in the center of the simulation domain. It is cooled and flows downwards along isothermal boundaries. At the Rayleigh number 10^6 (Fig. 1(a)), the fluid circulation is stable, forming two counter-rotating vortices. After the initial thermal transient, the system reaches steady-state conditions. Although dimensionless temperatures are higher at the Prandtl number 0.25, velocities are lower than in the case of the Prandtl number 0.6.

At the Rayleigh number 10^7 (Fig. 1(b)), the Rayleigh–Taylor instabilities, which are the result of intensive cooling at the top, cause a blob of cold fluid (or a thermal) from the upper boundary towards the center of the simulation domain. The thermal produces two additional and stable vortices in the upper half of the simulation domain. At both Prandtl numbers (0.25 and 0.6), the horizontal symmetry is preserved and the system still reaches its steady-state conditions at the end of the simulation.

At the Rayleigh number 10^8, the symmetry of the fluid circulation is broken. Steady-state conditions are not reached at the end of the simulation. In the case of the Prandtl number 0.6 the thermals at the upper boundary are stronger than in the case of the Prandtl number 0.25, where the unstable fluid behavior is mainly generated in the lower corners of the simulation domain. At the Prandtl number 0.6 the symmetry is mainly preserved in the lower half of the simulation domain.

At the Rayleigh number 10^9 (Fig. 1(c)), fluid flow and related heat transfer from the upper to the lower part of the simulation domain are squeezed into a very narrow and unstable boundary layer. The Rayleigh–Taylor instabilities at the upper boundary and the Kelvin–Helmholtz instabilities at the side boundaries cause first a local and then a global transition from laminar to turbulent motion. Fig. 1(c) clearly shows an intense but locally bounded influence of the upper wall

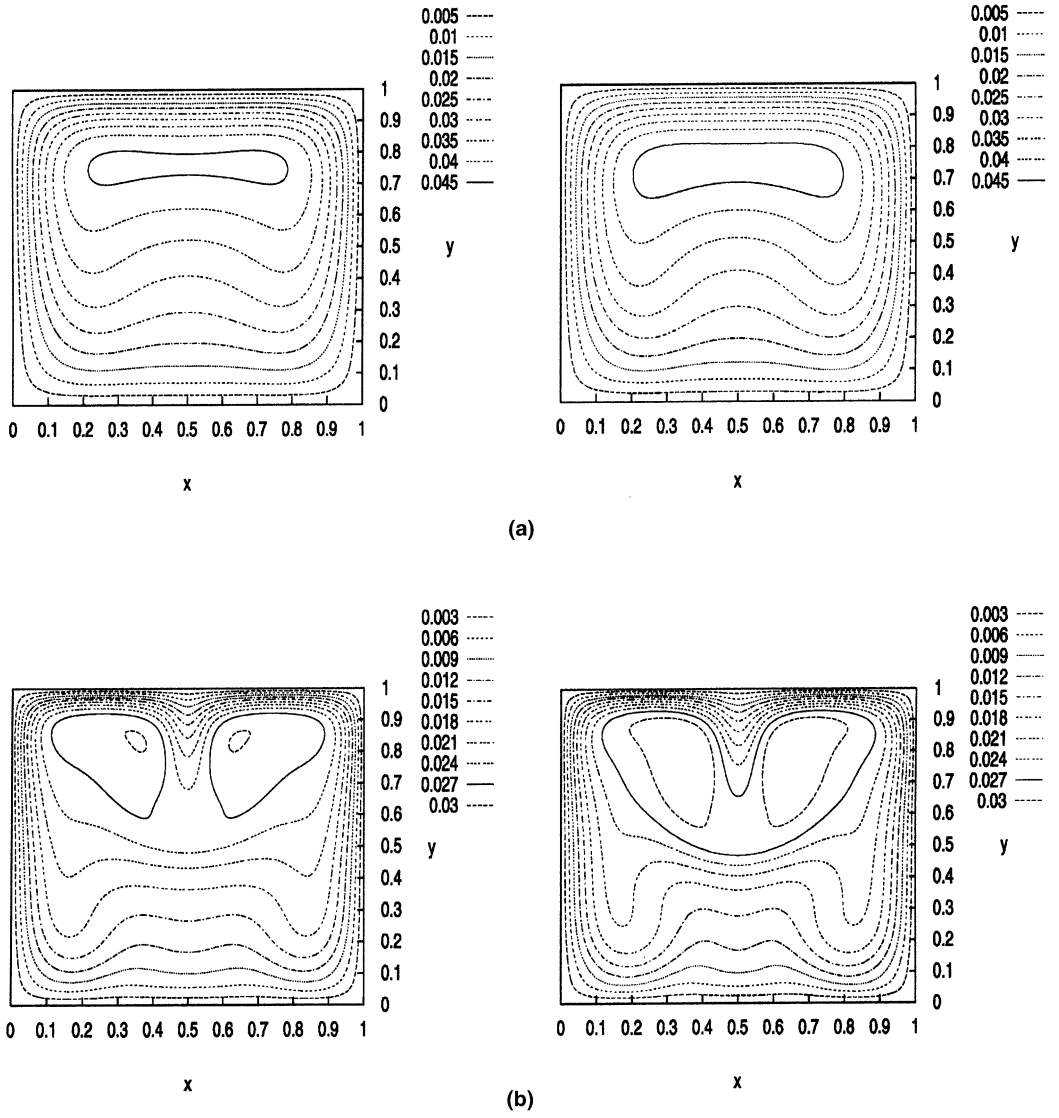

Fig. 1. Temperature field, $Pr = 0.6$ (left) and $Pr = 0.25$ (right). (a) $Ra = 10^6$, (b) $Ra = 10^7$, (c) $Ra = 10^9$, (d) $Ra = 10^{11}$ (figures indicate temperature values corresponding to isotherms).

thermals on the fluid circulation at Prandtl number 0.6, whereas the influence is much more global at the Prandtl number 0.25.

When the Rayleigh number is increased to 10^{11}, the flow in the entire simulation domain becomes unsteady with no permanent fluid structures (Fig. 1(d)). Due to these instabilities, the majority of thermal and kinetic energy is transported from the boundary layer flow into temporary fluid structures. Also, heat transfer on the boundaries of the simulation domain exhibits large random-like peaks and reductions of heat flow.

4.1. Time distributions of boundary-averaged Nusselt numbers

The simulation of the fluid behavior as a time-dependent system enables us to realistically determine the dimensionless heat transfer coefficient (Nusselt number) on the boundaries of the simulation domain. The Nusselt number was defined as:

$$Nu(t, x_b) = \frac{1}{(h(t)_{\text{vol.-aver.}} - h(t)_{\text{bound.-aver.}})} \frac{\partial h(t, x_b)}{\partial x_b}. \quad (17)$$

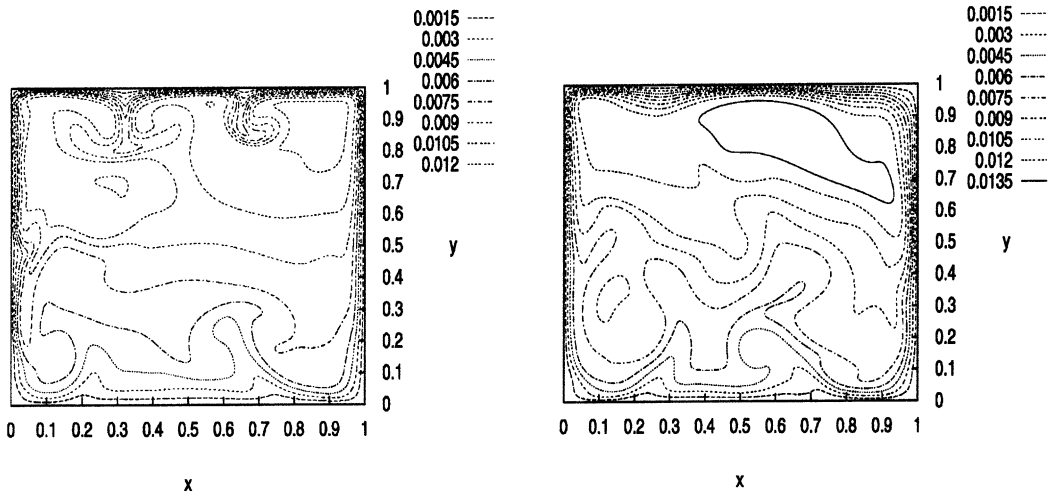

(c)

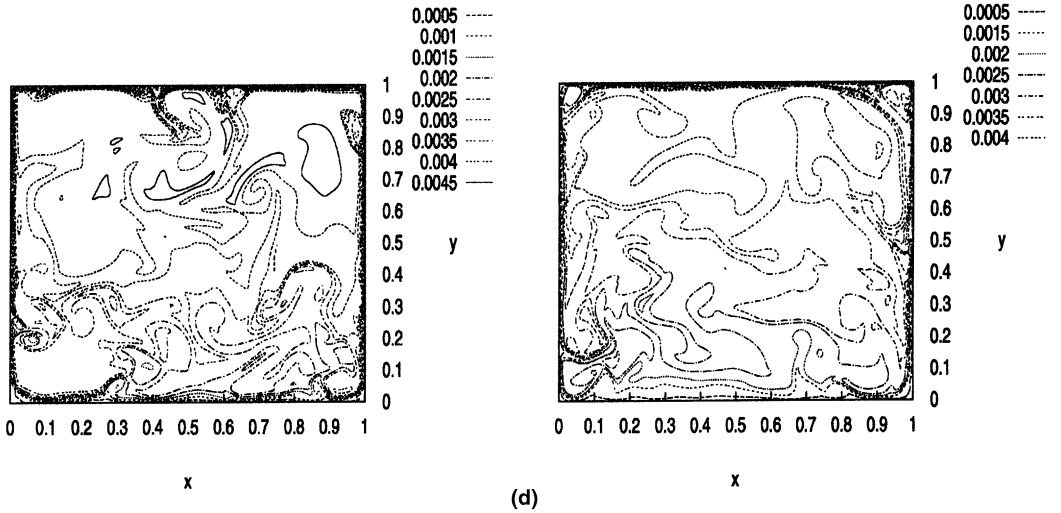

(d)

Fig. 1 (*continued*)

In general, Nusselt numbers increase when the Rayleigh number increases. As was already reported by Nourgaliev et al. [10], local Nusselt numbers are low at the bottom and increase towards the upper boundary of the simulation domain. A local maximum is reached in the upper corners of the sidewalls. Similar values of the local Nusselt number also appear on the upper boundary.

Fig. 2 presents the time distributions of the boundary-averaged Nusselt number, which is defined as:

$$Nu(t)_{\text{bound.-aver.}} = \frac{1}{L_b} \int_{L_b} Nu(t, x_b)\, dx_b. \tag{18}$$

The averaging was performed over 256 boundary grid points. Because the Nusselt number is formulated as a normalized temperature gradient (Eq. (17)), it is infinite at the beginning of the simulation.

At the Rayleigh number 10^6 (Fig. 2(a)), the time distributions of side and upper boundary-averaged Nusselt number indicate the appearance of the first bifurcation point between 0.05 and 0.1. At this point, marked with the Nusselt number disturbance, two counter-rotating vortices are formed ending the pure conduction regime. After the convection regime starts, the system soon reaches its steady state.

At the Rayleigh number 10^7, the formation of an additional vortex pair is reflected as a second disturbance in side and upper boundary-averaged Nusselt number distributions. When the Rayleigh number is increased to

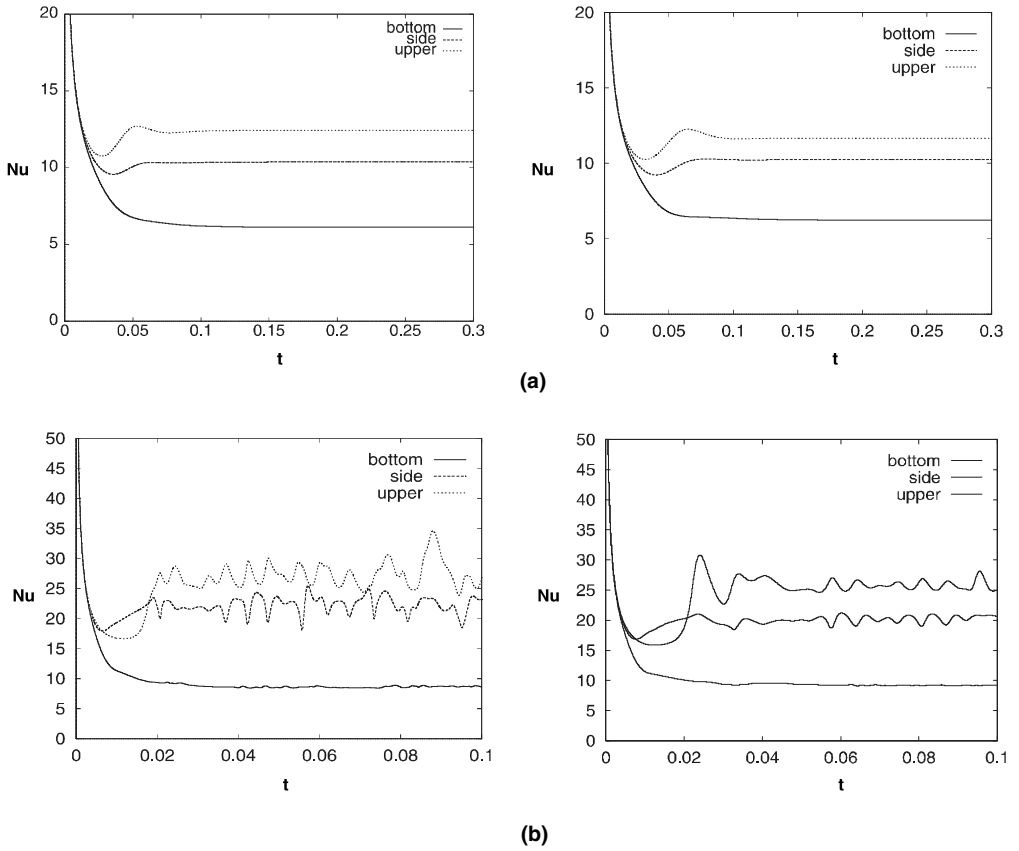

Fig. 2. Boundary-averaged Nusselt number, $Pr = 0.6$ (left) and $Pr = 0.25$ (right). (a) $Ra = 10^6$, (b) $Ra = 10^8$, (c) $Ra = 10^9$, (d) $Ra = 10^{11}$.

10^8 (Fig. 2(b)) the second vortex pair becomes unstable causing oscillations with almost uniform frequency in the upper part of the simulation domain. However, the bottom boundary Nusselt number distribution stays flat, reaching a steady state soon after the initial thermal transient.

At the Rayleigh number 10^9 (Fig. 2(c)), the time distributions of side and upper boundary-averaged Nusselt numbers reveal a stochastic nature of heat transfer for the Prandtl number 0.6 as well as 0.25. For the bottom boundary at the Prandtl number 0.6, the Nusselt number distribution stays almost flat through the entire simulation interval, whereas at the Prandtl number 0.25 the process of heat transfer also becomes unsteady at the bottom boundary.

At the Rayleigh number 10^{11} (Fig. 2(d)), the boundary-averaged Nusselt number time distributions for the bottom, side and upper boundary reveal turbulent fluid motion. Nusselt numbers on the side boundary nearly reach Nusselt numbers on the upper boundary. This is the result of the strong side and upper boundary layer thermals, which dominate the heat transfer process.

The comparison of the Nusselt number distributions for the Prandtl numbers 0.6 and 0.25 shows that lower Prandtl numbers enhance heat transfer through the bottom region, whereas higher Prandtl numbers enhance heat transfer through the upper region of the simulation domain.

4.2. Time-boundary-averaged Nusselt numbers

To compare the present results with those from other authors, time-boundary-averaged Nusselt numbers were also calculated. In this case, averaging was performed over the 256 boundary grid points and over more than 10 000 time integration steps:

$$Nu_{\text{time-bound.-aver.}} = \frac{1}{L_b}\frac{1}{T}\int_{L_b}\int_{T} Nu(t, x_b)\,\mathrm{d}t\,\mathrm{d}x_b. \tag{19}$$

The Rayleigh–Nusselt number dependencies are presented in $\log_{10} - \log_{10}$ diagrams and compared with results of other authors (Figs. 3–5).

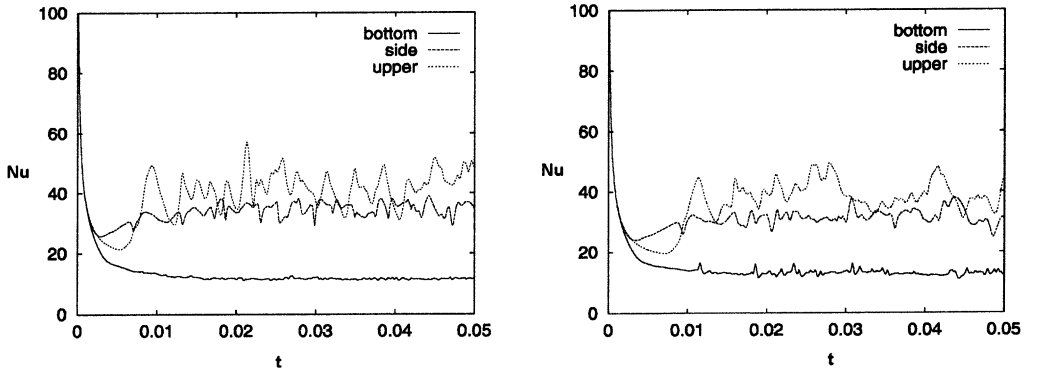

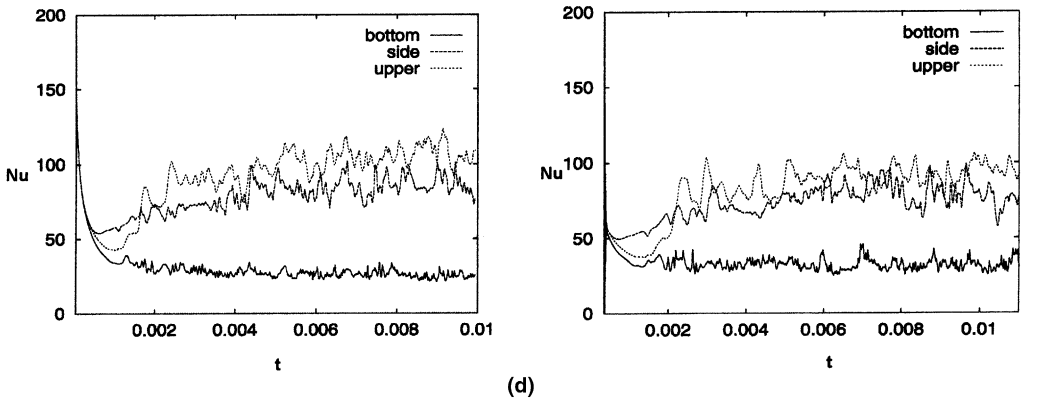

Fig. 2 (*continued*)

In general, as Figs. 3–5 reveal, the calculated values of the Nusselt number agree well with those already published. The discrepancies that do appear originate from differences in geometries, as found in the work of Kulacki and Goldstein [1] and Wörner et al. [14], or from higher Prandtl number, as used by Steinberner and Reineke [5].

It is widely accepted that the Rayleigh–Nusselt number relation is linear in a $\log_{10}-\log_{10}$ diagram and that the Prandtl number has no effect on the average Nusselt number (e.g. [24]). As Figs. 3–5 show, the Nusselt number behavior is much more complicated. On the bottom boundary (Fig. 3), the calculated Rayleigh–Nusselt number relation has a parabolic shape, which is more distinctive at higher Prandtl numbers. Also, on the side boundary (Fig. 4), the Rayleigh–Nusselt number relation is not linear. On the upper boundary (Fig. 5), there appear to be three separate regions, roughly in the ranges $Ra = 10^6$–10^7, 10^7–10^8 and 10^8–10^{11}, in which the Rayleigh–Nusselt number relation is linear with a different slope. The Rayleigh–Nusselt number relation thus qualitatively reflects the gradual change of the flow

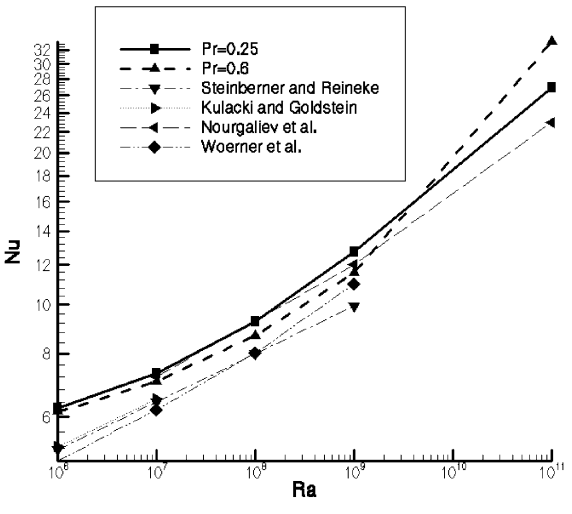

Fig. 3. Rayleigh number vs. Nusselt number on the bottom boundary.

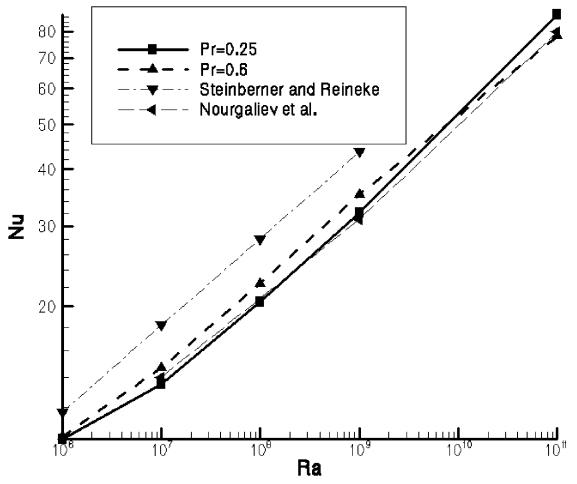

Fig. 4. Rayleigh number vs. Nusselt number on the side boundary.

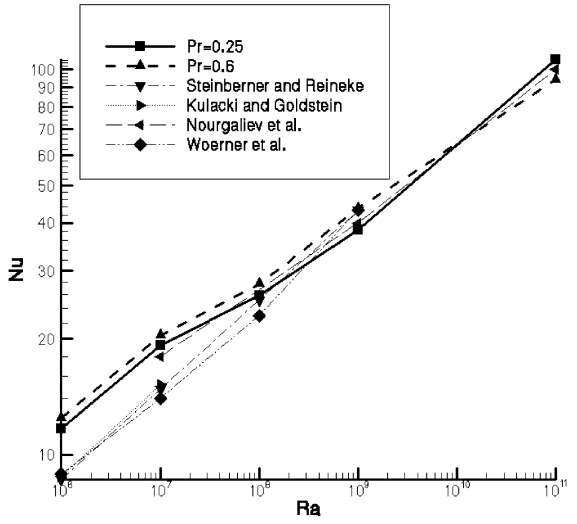

Fig. 5. Rayleigh number vs. Nusselt number on the top boundary.

from a laminar to a turbulent regime, when heat transfer on the wall becomes increasingly unsteady.

Differences in the Rayleigh–Nusselt number relation also exist for the two different Prandtl numbers used in our calculations. The diagram in Fig. 5 reveals that the threshold Rayleigh number where the transition from laminar to turbulent flow occurs is not significantly influenced by the fluid Prandtl number. Yet, the transition and the turbulent fluid motion exhibit higher-amplitude velocity and temperature fluctuations at a higher Prandtl number.

5. Conclusions

Two-dimensional numerical simulations of a fluid flow with internal heat generation in a square cavity at Rayleigh numbers from 10^6 to 10^{11} and at Prandtl numbers 0.25 and 0.6 were performed to investigate the Nusselt number behavior on the boundaries of the simulation domain. The dynamics of the Nusselt number was also analyzed to identify the influence of different flow regimes on boundary heat transfer. To capture the fluid subgrid motion in the turbulent regime, the LES Smagorinsky model was implemented. Although the simulation results prove that the Smagorinsky model is a robust and reliable numerical tool for solving turbulent natural convection cases in a fluid with an internal heat generation, we were not successful in finding any previous implementation of the Smagorinsky model for the presented problem.

Our simulations disclose that steady-state heat transfer can be achieved up to a Rayleigh number of 10^7. At the Rayleigh number 10^8, instabilities are observed, which result in an oscillating behavior of the system. When the Rayleigh number is further increased, the fluid flow becomes unsteady with no permanent fluid structures. Moreover, Nusselt number calculations reveal large intervals between the lowest and the highest time-averaged Nusselt numbers. It was also observed that a higher Prandtl number enhances heat transfer through the side and upper boundaries, whereas at a lower Prandtl number heat transfer is enhanced through the bottom boundary.

The calculated time distributions of boundary-averaged Nusselt numbers disclose the time of the first bifurcation point crossing. It was also observed that turbulence first appears locally, at the side and the upper boundaries, whereas the fluid flow in the lower region of the simulation domain stays laminar. Global turbulence does not appear up to a Rayleigh number 10^{11}. It was also found that the Prandtl number does not significantly influence the time of the laminar-to-turbulent flow transition. However, it has an important impact on the location and the intensity of turbulence.

A comparison of the time-boundary-averaged Nusselt number reveal that the present results in general agree well with those already published. Nevertheless, the simulations reveal that the Rayleigh–Nusselt number relation is not uniformly linear in the $\log_{10}$–$\log_{10}$ diagram, as has been widely accepted. The Rayleigh–Nusselt number relation reveals the regime changes. Furthermore, it was also observed that this process is distinctive at different boundaries of the simulation domain.

Acknowledgements

The authors wish to thank the anonymous reviewers for their valuable comments. The financial support of

the Ministry of Science and Technology of the Republic of Slovenia is also gratefully acknowledged.

References

[1] F.A. Kulacki, R.J. Goldstein, Thermal convection in a horizontal fluid layer with uniform volumetric energy sources, J. Fluid Mech. 55 (1972) 271–287.
[2] F.A. Kulacki, M.E. Nagle, Natural convection in a horizontal fluid layer with volumetric energy sources, J. Heat Transfer 97 (1975) 204–211.
[3] F.A. Kulacki, A.A. Emara, High Reynolds number convection in enclosed fluid layers with internal heat sources, US NRC Report NUREG-75/065, 1975.
[4] M. Jahn, H.H. Reineke, Free convection heat transfer with internal heat sources: calculations and measurements, in: Proceedings of the Fifth Internal Heat Transfer Conference, vol. 3, paper NC-2.8, Tokyo, Japan, 1974.
[5] U. Steinberner, H.H. Reineke, Turbulent buoyancy convection heat transfer with internal heat sources, in: Proceedings of the Sixth Internal Heat Transfer Conference, vol. 2, Toronto, Canada, 1978, pp. 305–310.
[6] F. Mayinger, M. Jahn, H.H. Reineke, V. Steinbrenner, Examination of thermohydraulic processes and heat transfer in a core melt, BMFT RS 48/1, 1976, Institut fuer Verfahrenstechnic der T.U., Hannover, Germany, 1976.
[7] F.J. Asfia, B. Frantz, V.K. Dhir, Experimental investigation of natural convection heat transfer in volumetrically heated spherical segments, J. Heat Transfer 118 (1996) 31–37.
[8] B. Frantz, V.K. Dhir, Experimental investigation of natural convection heat transfer in spherical segments of volumetrically heated pools, in: Proceedings of National Heat Transfer Conference, vol. 192, San Diego, CA, 1992, pp. 69–72.
[9] S.S Abalin, V.G. Asmolov, V.D. Daragan, E.K. D'yakov, A.V. Merzlyakov, V.Y. Vishnevsky, Kinematic viscosity measurements of C-100 and C-22 corium, OECD RASPLAV project, RP-TR-18, 1996.
[10] R.R. Nourgaliev, T.N. Dinh, B.R. Sehgal, Effect of fluid Prandtl number on heat transfer characteristics in internally heated liquid pools with Rayleigh number up to 10^{12}, Nucl. Eng. Des. 169 (1997) 165–184.
[11] R. Verzicco, R. Camussi, Prandtl number effects in convective turbulence, J. Fluid Mech. 383 (1999) 55–73.
[12] T.N. Dinh, R.R. Nourgaliev, Turbulence modeling for large volumetrically heated liquid pools, Nucl. Eng. Des. 169 (1997) 131–150.
[13] O. Kymäläinen, H. Tuomisto, O. Hongisto, T.G. Theofanous, Heat flux distribution from volumetrically heated pool with high Rayleigh number, in: Proceedings of the Sixth International Topical Meeting on Nuclear Reactor Thermal Hydraulics, NURETH-6, Grenoble, France, 1993, pp. 47–53.
[14] M. Wörner, M. Schmidt, G. Grötzbach, Direct numerical simulation of turbulence in an internally heated convective fluid layer and implications for statistical modelling, J. Hydraul. Res. 35 (6) (1997) 773–797.
[15] B.R. Sehgal, T.N. Dinh, R.R. Nourgaliev, G. Kolb, A. Karbojian, V.A. Bui, Research at RIT on thermal loading on, and mechanical response of, a reactor vessel during severe accident, Cooperative Severe Accident Research Program CSARP'98 "Lower head integrity", USA, May 1998.
[16] W.J. Decker, Numerical studies of bifurcations and chaos in natural convection, Ph.D. Thesis, University of Virginia, VA, 1996.
[17] A. Horvat, Modeling of natural convection phenomena in nuclear reactor core melt, M.Sc. Thesis, Faculty of Mathematics and Physics, University of Ljubljana, Ljubljana, Slovenia, 1998, http://www2.ijs.si/~ahorvat.
[18] T.M. Eidson, Numerical simulation of the turbulent Rayleigh–Bénard problem using subgrid modeling, J. Fluid Mech. 158 (1985) 245–268.
[19] J.O. Hinze, Turbulence, second ed., McGraw-Hill, New York, 1959, p. 23.
[20] S.V. Patankar, D.B. Spalding, Heat and Mass Transfer in Boundary Layers, second ed., Intertext Books, London, 1970, p. 21.
[21] M. Germano, U. Piomelli, P. Moin, W.H. Cabot, A dynamic subgrid-scale eddy viscosity model, Phys. Fluids A 4 (3) (1992) 633–635.
[22] D.K. Lilly, A proposed modification of the Germano subgrid-scale closure method, Phys. Fluids A 3 (7) (1991) 1760–1765.
[23] S.-H. Peng, L. Davidson, Comparison of subgrid-scale models in LES for turbulent convection flow with heat transfer, in: Proceedings of the Second Turbulent Heat Transfer Conference, vol. 1, Manchester, UK, 1998, pp. 5.25–5.35.
[24] T.G. Theofanous, C. Liu, S. Additon, S. Angelini, O. Kymäläinen, T. Salmassi, In-vessel coolability and retention of a core melt, Nucl. Eng. Des. 169 (1997) 1–49.
[25] F.J. Asfia, V.K. Dhir, An experimental study of natural convection in a volumetrically heated spherical pool bounded on the top with rigid wall, Nucl. Eng. Des. 163 (1996) 333–348.
[26] V.S. Arpaci, Buoyant turbulent flow driven by internal energy generation, Int. J. Heat Mass Transfer 38 (15) (1995) 2761–2770.
[27] R. LeVeque, High-resolution finite volume method on arbitrary grids via wave propagation, J. Comp. Phys. 78 (1988) 36–63.
[28] C. Hirsch, Numerical Computation of Internal and External Flows, vol. 1, Wiley, New York, 1988, pp. 422–504.
[29] C.A.J. Fletcher, Computational Techniques for Fluid Dynamics, vol. 2, Springer, Berlin, 1988, p. 340.
[30] W.H. Press, S.A. Teukolsky, W.T. Vetterling, B.P. Flannery, Numerical Recipes in C, The Art of Scientific Computing, second ed., Cambridge University Press, Cambridge, 1997, p. 877.